Mon. Not. R. Astron. Soc. **000**, 1–17 (2012) Printed 21 February 2022 (MN LATEX style file v2.2)

Spectral Energy Distributions of Type 1 AGN in XMM-COSMOS Survey II - Shape Evolution

Heng Hao[1,2⋆], Martin Elvis[2], Francesca Civano[2,3], Gianni Zamorani[4], Luis C. Ho[5], Andrea Comastri[4], Marcella Brusa[6,7], Angela Bongiorno[6,8], Andrea Merloni[6], Jonathan R. Trump[9], Mara Salvato[10,11], Chris D. Impey[12], Anton M. Koekemoer[13], Giorgio Lanzuisi[6], Annalisa Celotti[1,14,15], Knud Jahnke[16], Cristian Vignali[4,7], John D. Silverman[17], C. Megan Urry[18], Kevin Schawinski[19], Peter Capak[20]

[1] *SISSA, Via Bonomea 265, I-34136 Trieste, Italy*
[2] *Harvard-Smithsonian Center for Astrophysics, 60 Garden Street, Cambridge, MA 02138, USA*
[3] *Dartmouth College, Department of Physics and Astronomy, 6127 Wilder Lab, Hanover, NH 03755*
[4] *INAF-Osservatorio Astronomico di Bologna, via Ranzani 1, I-40127 Bologna, Italy*
[5] *The Observatories of the Carnegie Institute for Science, Santa Barbara Street, Pasadena, CA 91101, USA*
[6] *Max Planck Institute für Extraterrestrische Physik, Postfach 1312, 85741, Garching bei München, Germany*
[7] *Dipartimento di Fisica e Astronomia, Università degli studi di Bologna, viale Berti Pichat 6/2 40127 Bologna Italy*
[8] *INAF-Osservatorio Astronomico di Roma, Via di Frascati 33, 00040, Monteporzio Catone, Rome, Italy*
[9] *UCO/Lick Observatory, University of California, Santa Cruz, CA 95064, USA*
[10] *IPP - Max-Planck-Institute for Plasma Physics, Boltzmann Strasse 2, D-85748, Garching bei München, Germany*
[11] *Excellence Cluster, Boltzmann Strasse 2, D-85748, Garching bei München, Germany*
[12] *Steward Observatory, University of Arizona, 933 North Cherry Avenue, Tucson, AZ 85721, USA*
[13] *Space Telescope Science Institute, 3700 San Martin Drive, Baltimore, MD 21218, USA*
[14] *INAF - Osservatorio Astronomico di Brera, via E. Bianchi 46, I-23807 Merate, Italy*
[15] *INFN - Sezione di Trieste, via Valerio 2, 34127, Trieste, Italy*
[16] *Max-Planck-Institut für Astronomie, Königstuhl 17, Heidelberg, D-69117, Germany*
[17] *Kavli Institute for the Physics and Mathematics of the Universe, Todai Institutes for Advanced Study, the University of Tokyo, Kashiwa, Japan 277-8583 (Kavli IPMU, WPI)*
[18] *Physics Department and Yale Center for Astronomy and Astrophysics, Yale University, New Haven, CT 06511, USA*
[19] *Institute for Astronomy, Department of Physics, ETH Zurich,Wolfgang-Pauli-Strasse 16, CH-8093 Zurich, Switzerland*
[20] *California Institute of Technology, MC 105-24, 1200 East California Boulevard, Pasadena, CA 91125, USA*

Version Nov 18th, 2013.

ABSTRACT

The mid-infrared to ultraviolet (0.1 – 10 μm) spectral energy distribution (SED) shapes of 407 X-ray-selected radio-quiet type 1 AGN in the wide-field "Cosmic Evolution Survey" (COSMOS) have been studied for signs of evolution. For a sub-sample of 200 radio-quiet quasars with black hole mass estimates and host galaxy corrections, we studied their mean SEDs as a function of a broad range of redshift, bolometric luminosity, black hole mass and Eddington ratio, and compared them with the Elvis et al. (1994, E94) type 1 AGN mean SED. We found that the mean SEDs in each bin are closely similar to each other, showing no statistical significant evidence of dependence on any of the analyzed parameters. We also measured the SED dispersion as a function of these four parameters, and found no significant dependencies. The dispersion of the XMM-COSMOS SEDs is generally larger than E94 SED dispersion in the ultraviolet, which might be due to the broader "window function" for COSMOS quasars, and their X-ray based selection.

Key words: galaxies: evolution; quasars: general; surveys

1 INTRODUCTION

The physical details of the continuum emission of Active Galactic Nuclei (AGN) remain unsettled after several

⋆ E-mail:henghao@post.harvard.edu

decades of study. Yet, understanding the continuum emission of AGN, from X-rays to radio, is essential to unlocking the physics of accretion onto super massive black holes (SMBHs). The continuum in each spectral region can be ascribed to distinct energy generation mechanisms: jets in the radio (see e.g. the review by Harris & Krawczynski 2006), dust in the infrared (IR, McAlary & Rieke 1988; Sanders et al. 1989), accretion disks in the optical-ultraviolet (UV) and soft X-rays (Shakura & Sunyaev 1973; Rees 1984; Czerny & Elvis 1987), and Compton up-scattering by hot coronae in the hard X-rays (e.g., Zamorani et al. 1981; Laor et al. 1990; Haardt & Maraschi 1991; Williams et al. 1992; Zdziarski et al. 2000; Kawaguchi et al. 2001; Mateos et al. 2005; Mainieri et al. 2007).

Continuum changes with redshift, luminosity or Eddington ratio might be expected. Most SMBH growth occurs during the active 'AGN' phases (the 'Soltan argument', Soltan 1982), implying that most galaxy bulges went through an AGN phase (e.g. Magorrian et al. 1998). Rapid growth of central SMBHs happens in high-redshift and high-luminosity quasars emitting near the Eddington limit (Barth et al. 2003; Vestergaard 2004; Jiang et al. 2006; Kurk et al. 2007; but see also Steinhardt & Elvis 2010). The space density of X-ray-selected, highly luminous AGN peaks at around $z = 2.5$, and declines at $z > 3$ (Silverman et al. 2005, Brusa et al. 2009, Civano et al. 2011). Low-luminosity AGN are more prevalent at $z < 1$ than higher luminosity ones (Cowie et al. 2003; Fiore et al. 2003; Ueda et al. 2003; Silverman et al. 2005). As the central SMBH is the driver of the emission, one might expect the quasar SED to evolve as the black hole grows due to accretion.

Many parameters – the black hole mass, the AGN luminosity relative to the host galaxy, the accretion rate, the physical properties of the accretion disk and the properties of the absorbing dust – might affect the shape of the AGN SED (Wilkes 2003). For instance, the optical to X-ray spectral index [α_{OX}=0.384log($F_{2keV}/F_{2500\mathring{A}}$)], correlates with luminosity but not with redshift (e.g. Vignali et al. 2003a; Steffen et al. 2006; Just et al. 2007; Young et al. 2010; Lusso et al. 2010). It is possible that similar dependency of luminosity in the SED shape exists at other wavelengths.

Observations indicate a tight link between SMBH growth and galaxy evolution (e.g. Magorrian et al. 1998; Marconi & Hunt 2003; Tremaine et al. 2002; Menci et al. 2008). Locally, SMBHs appear to reside at the center of most galaxies and the SMBH masses are tightly correlated with their masses (e.g. Kormendy & Richstone 1995; Marconi & Hunt 2003) and velocity dispersions (i.e. $M_{BH} - \sigma$ relations; Ferrarese & Merritt 2000; Gebhardt et al. 2000; Tremaine et al. 2002). Some evidence for evolution of this relationship has been reported using several methods (e.g. Peng et al. 2006; Shields et al. 2006; Ho 2007; Merloni et al. 2010). This evolution would imply that the feedback of the SMBH to the host galaxy evolves. Similar evolution in the innermost regions (within the torus) is possible too. All of these processes could lead to different SED shapes.

However, no evolution of the AGN SED has yet been demonstrated. There is no convincing evidence for any change of SED with redshift (Silverman et al. 2002; Mathur et al. 2002; Brandt et al. 2002; Vignali et al. 2003b). High redshift quasars (up to redshift 7) show optical spectra similar to low redshift quasars from the SDSS (Jiang et al. 2007, Mortlock et al. 2011). There is evidence, though, that the SEDs of extremely low-luminosity ($L_{bol} \lesssim 10^{42}\ erg/s$) nuclei are remarkably different from those of luminous ($L_{bol} \gtrsim 10^{44}\ erg/s$) AGN (Ho 1999, 2008).

So far, the systematic study of the dependency of the SED shape with physical parameters has been limited by difficulty in obtaining a large sample size with good multi-wavelength coverage. The Cosmological Evolution Survey (COSMOS, Scoville et al. 2007) has the appropriate combination of depth, area and extensive multi-wavelength data that allows for a sensitive survey of AGN to address this question.

The COSMOS field has been imaged with XMM-Newton for a total of ~ 1.5 Ms (Hasinger et al. 2007; Cappelluti et al. 2007, 2009). Optical identifications were made by Brusa et al. (2010) for the entire XMM-COSMOS sample. Photometric properties and redshifts were produced for each point source. This extensive data set allows us to make a systematic study of the evolution of the SED shape, which is the main purpose of this paper.

From this complete sample, we extracted a sample of 413 type 1 AGN (broad emission line FWHM>2000 km s^{-1}). The type 1 AGN SED sample catalog is described in detail in Elvis et al. (2012, hereafter Paper I). It includes quasars with redshifts $0.1 \leqslant z \leqslant 4.3$ and magnitudes $16.9 \leqslant i_{AB} \leqslant 24.8$, with 98% of the sources being radio-quiet (Hao et al. 2013b). This sample is twenty times larger than the Elvis et al. (1994, hereafter E94) radio-quiet type 1 AGN SED sample, and has full wavelength coverage from radio to X-rays (for a total of 43 photometric bands, Paper I) and high confidence level spectroscopic redshifts (Trump et al. 2009a; Schneider et al. 2007; Lilly et al. 2007, 2009). The mean SED of the XMM-COSMOS type 1 AGN was calculated and compared to previous studies: E94, Richards et al. (2006, hereafter R06), Hopkins et al. (2007) and Shang et al. (2011) in paper I Figure 21. In this figure we can see, in the near-IR to optical-UV range, all recent studies have very similar shapes to E94, while the XMM-COSMOS mean host-corrected quasar SED has a less prominent 'big-blue bump', possibly due to remnant host contributions, not corrected because of the dispersion in the black hole mass and host luminosity scaling relationship itself. In this paper, we compare the Paper I sample with E94 as a representative.

Paper I presented the selection and properties of the XMM-COSMOS type 1 AGN sample of 413 quasars (XC413 hereinafter). We used various radio-loud criteria ($R_L = \log(f_{5GHz}/f_B) > 1$, Wilkes & Elvis 1987; $q_{24} = \log(f_{24\mu m}/f_{1.4GHz}) < 0$, Appleton et al. 2004; $R_{1.4} = \log(f_{1.4GHz}/f_J)$, in the observed frame; $q_{24,obs}$, the q_{24} in the observed frame; $R_{uv} = \log(f_{5GHz}/f_{2500\mathring{A}}) > 1$, Stocke et al. 1992; $P_{5GHz} = \log[P_{5GHz}(W/Hz/Sr)] > 24$, Goldschmidt et al. 1999; and $R_X = \log(\nu L_\nu(5GHz)/L_X) > -3$, Terashima & Wilson 2003) to define a radio-loud quasar. We find that the radio-loud fraction is 1.5%–4.5% using any criterion, except R_{uv}, which is subject to reddening and host contamination issues (Hao et al. 2013b). Using two criteria at the same time, the radio-loud fraction is $\lesssim 8/413 = 2\%$. Only 6 XC413 quasars satisfy all the seven criteria. We define these 6 quasars in this catalog as radio-loud (Paper I; Hao et al. 2013). We refer to the radio-quiet sub-sample of XC413 as XCRQ407 hereinafter.

Estimates of black hole mass (M_{BH}) for 206 of XC413

Table 1. Source Properties in Parameter Space[1]

XID	z[a]	logM_{BH}[b] [$M_\odot$]	logL_{bol}[c] [erg s^{-1}]	λ_E[d]	logL_{all}[e] [erg s^{-1}]	L_{ir}/L_{all}[f] %	L_{opt}/L_{all}[g] %	L_X/L_{all}[h] %	L_{bol}/L_{opt}	log$L_{bol,hc}$[i] [erg s^{-1}]	$L_{bol,hc}/L_{opt,hc}$
1	0.373	8.58	45.36	0.048	45.46	19.2	37.1	5.6	2.11	...	...
2	1.024	8.96	45.82	0.056	46.09	32.5	17.8	27.6	2.98	45.79	3.35
3	0.345	8.66	45.18	0.026	45.39	33.8	24.1	17.2	2.56	45.11	3.44
4	0.132	7.31	44.25	0.068	44.55	40.8	35.5	3.0	1.41	44.19	1.50
5	1.157	...	45.95	...	46.21	34.2	25.2	12.8	2.18	...	...
6	0.360	8.64	44.89	0.014	45.20	31.1	34.7	4.7	1.42	44.74	1.71
7	0.519	8.38	45.21	0.053	45.44	37.6	27.5	17.9	2.13	45.16	2.46
8	0.699	7.96	45.78	0.518	45.97	33.2	32.2	7.3	2.00	45.78	1.98
9	1.459	8.86	45.90	0.088	46.28	40.1	18.4	11.7	2.30	45.89	2.43
...	...	...	...	...	...	...	...	...	...	...	...

[1] A portion of the table is shown here for guidance. The complete table will be available online.

[a] The spectroscopic redshifts are from Trump et al. (2009a), Schneider et al. (2007), Lilly et al. (2007, 2009)
[b] The black hole mass estimates are from Trump et al. (2009b) and Merloni et al. (2010)
[c] Calculated by integrating the rest frame SED from 1 μm to 40 keV.
[d] $\lambda_E = L_{bol}/L_{Edd}$, details in § 2.3.
[e] Calculated by integrating the rest frame SED from 1.4 GHz to 40 keV.
[f] L_{ir} is calculated by integrating the rest frame SED from 24 μm to 1 μm.
[g] L_{opt} is calculated by integrating the rest frame SED from 1 μm to 912Å.
[h] L_X is calculated by integrating the rest frame SED from 0.5 keV to 40 keV.
[i] Calculated by integrating the rest frame host-corrected SED from 1 μm to 912Å for 203 quasars in the XMM-COSMOS sample.

have been made by Merloni et al. (2010) and Trump et al. (2009b). Both papers used single-epoch spectra and applied the scaling relations from reverberation mapping found by Vestergaard & Peterson (2006). This method requires high S/N spectra with the broad emission line not near the ends of the spectra. For the quasars with only zCOSMOS spectra, the black hole mass was estimated only for those with MgII lines in the spectra (Merloni et al. 2010), using the calibration of McLure & Jarvis (2002). 206 quasars out of XC413, and 203 quasars out of XCRQ407 have black hole mass estimates. Paper I estimated the host galaxy contribution for 203 of these 206 quasars using the scaling relationship between black hole mass and host luminosity (Marconi & Hunt 2003) adding an evolutionary term (Bennert et al. 2010, 2011), excluding the 3 which had over-subtraction problems (the estimated host galaxy luminosity is larger than the observed luminosity). We define this sub-sample (SS) as SS203. In SS203, 200 quasars are radio-quiet. We refer to this subsample as SSRQ200.

In Paper I, the rest frame SEDs of XC413 were constructed on a uniform frequency grid ($\Delta \log \nu = 0.02$) from radio to X-rays. As there is limited data in the far-IR ($> 10\mu m$ in rest frame) and longer wavelengths, and because the UV flux is strongly affected by both variability and strong broad emission lines, we defer the analysis of these regions to a later paper. In this paper, we focus on the SED shape in the optical to mid-IR range (0.1 – 10 μm), while all the plots are shown in the rest frame $0.1 - 10\mu m$ range. Note that all the sources discussed in this paper are broad line AGN with typical luminosity ($\sim 10^{44} - 10^{47}$erg/s), typical black hole mass ($\sim 10^7 - 10^9 M_\odot$) and typical accretion rates (Eddington ratio larger than 0.01, see in § 2.3).

All the wavelengths discussed in this paper are in the rest frame. We adopt the WMAP 5-year cosmology (Komatsu et al. 2009), with H_0 =71 km s^{-1} Mpc^{-1}, $\Omega_M = 0.26$ and Ω_Λ= 0.74.

2 PARAMETER SPACE

2.1 Bolometric Luminosity

The bolometric luminosity is the total energy per second radiated by the quasar at all wavelengths in all directions. This luminosity is, in principle, simply calculated by directly integrating the rest-frame SED over the whole wavelength range. In practice, this is difficult and observationally expensive. For the sample discussed in this paper, it is possible to approximate the bolometric luminosity with the SEDs available (Paper I).

As described in Paper I, the SEDs are produced by linearly interpolating between the data points in $\log \nu L_\nu$ versus $\log \nu$ space (i.e. connecting the individual points with power laws in linear space). The COSMOS photometry for the XC413 sample is >90% complete from u (CFHT) to MIPS 24μm, that is over the 1.8 dex wide 0.35μm – 24μm ($\sim$0.14μm – 10μm for the typical z = 1.5 of XC413) observed frame interpolation is unproblematic (Paper I). In the mid-infrared range, for quasars with 70μm or 160μm detections, we joined the 24μm data to the longer wavelength points with a power-law in log νf_ν vs. log ν space; for the others we extrapolated from the rest frame 24μm to 8μm slope and checked that the extrapolation generally works. As the far-IR to radio photometry data are sparse, for each source with a $> 3\sigma$ VLA detection, we assumed a power law $f_\nu \propto \nu^{-0.5}$ (e.g., Ivezić 2004) in the rest frame 1.4 GHz (21 cm) to 100 GHz (3 mm) range. In the 100 GHz (3 mm) to 160μm part, the SED can be approximated by the red end of the grey body $f_\nu \propto \nu^{3+\beta}/(e^{h\nu/kT} - 1)$, when $h\nu \ll kT$, $f_\nu \propto \nu^{2+\beta}$

(e.g. Lapi et al. 2011). β is generally chosen in the range 1–2 (Dunne & Eales 2001). We thus choose $\beta = 1$, i.e. we assume a power-law $f_\nu \propto \nu^3$ in this wavelength range. We directly linearly interpolate from Lyman break (1216Å) and 0.5 keV SED in $\log \nu L_\nu$ versus $\log \nu$ space (Laor et al. 1997). In the X-rays, we use the measured photon spectral index (Γ, $f_\nu \propto \nu^{(1-\Gamma)}$, Mainieri et al. 2007) and the observed 2 keV luminosity to get the SED in the 0.5 keV-40 keV (rest-frame), which is the range of the XMM data for XC413.

We used the SEDs from Paper I to calculate two approximations to the bolometric luminosities by integrating the rest frame SED over different wavelength ranges: (1) from 1 μm to 40 keV as L_{bol}; (2) from 21 cm/1.4 GHz to 40 keV as L_{all}. L_{all} was integrated over all the wavelengths for which we have data.

As the great majority of the XC413 quasars are radio-quiet and the photometric coverage from 24 μm to 1.4 GHz is currently sparse (Paper I), using L_{all} requires unwarranted extrapolation. The contribution of the radio emission to the bolometric luminosity is less than 3% even for the radio-loud sources. Most of the far-IR (at $\gtrsim 100\mu m$) luminosity is probably due to star-forming activity not the AGN (Netzer et al. 2007, Mullaney et al. 2012; but see Ho 2005). From the optical short-ward the primary emission is from the innermost region of the quasar (SMBH and accretion disk). The near and mid-IR continuum is the result of reprocessing shorter wavelength radiation of the quasar by dust (Sanders et al. 1989; Suganuma et al. 2006). The reprocessed dust emission thereby includes reprocessed primary radiation emitted in directions different from our line-of-sight. In a non-spherical geometry, as is likely present in quasars, this makes us count more radiation that we would in a 4π averaged calculation. In this sense, we are double-counting the primary emission (e.g. Lusso et al. 2010). Hence, L_{bol} which integrates from 1 μm to 40 keV is a good approximation of the true bolometric quasar luminosity defined over the entire wavelength range.

We note that directly integrating the SED in the rest frame from $1\mu m$ to 40 keV overestimates the quasar emission as the contribution from the host galaxy is not excluded. In practice, we do not have good estimates of the host contribution. For SSRQ200, we calculated the bolometric luminosity by integrating the host corrected SED from $1\mu m$ to 912Å as $L_{bol,hc}$ (last column in Table 1). As discussed in Paper I, we applied the scaling relationship between black hole mass and host luminosity reported in Marconi & Hunt (2003), and added an evolutionary term (Bennert et al. 2010, 2011), to estimate the contribution of host galaxy.

We note that L_{bol} will underestimate the total emission for three reasons: (1) excluding the IR to radio emission; (2) excluding the hard X-ray emission, where we do not have data; (3) ignoring the reddening of the primary emission in the optical/UV. Note that most, if not all, of these factors are not significant underestimate. For example, as we stated above, the contribution of the radio emission to the bolometric luminosity s less than 3% even for the radio-loud quasars.

To investigate the contribution to bolometric luminosity in different wavelength ranges, we calculated L_{ir} by integrating from 24 μm to 1 μm, L_{opt} from 1 μm to 912 $\mathring{A}$ and L_X from 0.5 keV to 40 keV. The fractions of the luminosity in different wavelength ranges are reported in Table 1 (The full table is available on line). Table 2 shows the median values and the ranges for L_{bol}, the fractions in three wavelength ranges, and the median values and the ranges for M_{BH} and Eddington ratio (which will be discussed in § 2.3). In general, the IR component ($1 - 24$ μm) provides an equal or greater contribution compared to the optical/UV 'big blue bump' component ($0.1 - 1$ μm). We also calculate the ratio of L_{bol} over L_{opt} as listed in Table 1 & 2. The mean L_{bol}/L_{opt} is 2.04 ± 0.75 (for XCRQ407) and 2.00 ± 0.71 (for SSRQ200) respectively. The mean $L_{bol,\ hc}/L_{opt,\ hc}$ is 2.11 ± 0.91. These values are larger than the ratio for E94 template (1.86) and for R06 template (1.61). This is probably caused by the selection effect, that E94 and R06 are optical selected samples that select more quasars with large optical contribution.

Table 2. Parameter Range

Parameter	XCRQ407			SSRQ200		
	min	med	max	min	med	max
z	0.10	1.57	4.26	0.13	1.50	4.26
$\log(M_{BH}/M_\odot)$	···	···	···	7.18	8.39	9.34
$\log L_{bol}$ (erg/s)	44.01	45.49	46.91	44.25	45.56	46.91
$\log L_{all}$ (erg/s)	44.29	45.71	47.40	44.55	45.77	47.40
L_{ir}/L_{all}	12.7%	33.2%	76.7%	12.7%	33.4%	76.7%
L_{opt}/L_{all}	2.1%	32.0%	60.5%	9.0%	31.8%	58.9%
L_X/L_{all}	0.33%	8.3%	43.9%	0.47%	8.1%	43.9%
L_{bol}/L_{opt}	1.10	1.90	8.30	1.10	1.84	8.30
λ_E	···	···	···	0.008	0.114	2.505
$\log L_{bol,\ hc}$ (erg/s)	···	···	···	44.19	45.53	46.86
$L_{bol,\ hc}/L_{opt,\ hc}$	···	···	···	1.11	1.94	11.48

2.2 Bolometric Correction

We then calculated the bolometric correction at various frequencies. The bolometric correction ($BC_\nu = L_{bol}/\nu L_\nu$) is the factor which transforms the luminosity in one band to the bolometric luminosity. As the host galaxy contribution is prominent for X-ray-selected quasars, we calculated the frequency-dependent BC in the rest frame 0.1–10μm only for SSRQ200 after performing the host correction. The bolometric correction was calculated for a $\Delta \log \nu = 0.02$ grid. The bolometric luminosity used in the calculation is $L_{bol,hc}$, which is the integration of host-corrected SEDs, listed as the last column in Table 1.

The mean and dispersion of the BC_ν are listed in Table 3 and shown in Figure 1, where we also show the mean and dispersion of the BC_ν for quasars at different redshift bins. The mean BC_ν curves for different redshift bins are consistent with each other given the large dispersion at each wavelength (Figure 1). The dispersion is largest at around 1 μm, where the host contribution is the highest, and in the extreme UV, where quasar variability is likely to contribute significantly to the observed dispersion.

For comparison, we plot the E94 mean SED bolometric correction as the cyan solid line in Figure 1. Hopkins et al. (2007) used a double power law to approximate the B band bolometric correction.

$$\frac{L_{bol}}{L_B} = 6.25 \left(\frac{L_{bol}}{10^{10} L_\odot}\right)^{-0.37} + 9.00 \left(\frac{L_{bol}}{10^{10} L_\odot}\right)^{-0.012}$$

To compare with the bolometric correction we got, we use

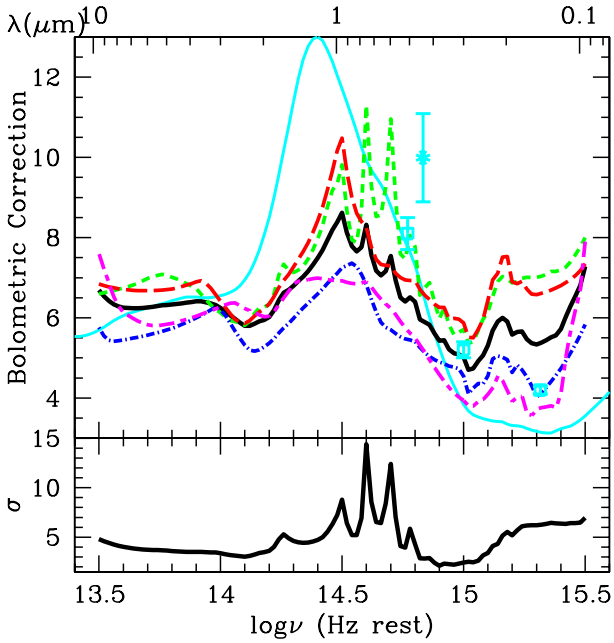

Figure 1. The frequency dependent bolometric correction for the SSRQ200 sample (black solid). The bolometric corrections in different redshift bins are also shown in the same plot (redshift: 0.1–1.2= green short dashed line, 50 quasars; 1.2–1.5= red long dashed line, 50 quasars; 1.5–1.8= blue dot dashed line, 51 quasars; and 1.8–4.3= magenta short long dashed line, 49 quasars). The cyan solid line show the bolometric correction for E94 RQ mean SED. The cyan star point at B band (4400Å) show the bolometric correction calculate from the Hopkins et al. (2007), assuming $\log L_{bol} = 45.5\ erg/s$, which is the median L_{bol} of SSRQ200. The cyan square show the bolometric correction at 3000Å and 5100Å respectively from Runnoe et al. (2012). In the bottom panel we show the dispersion of the bolometric correction for the SSRQ200 sample.

the median value of L_{bol} ($10^{45.5}\ erg/s$) in SSRQ200 to apply to the formula. The B band bolometric correction from Hopkins et al. (2007) is thus 9.99 (red star in Figure 1). More recently, Runnoe et al. (2012) studied the SEDs of 63 bright quasars at low redshift and found a linear bolometric correction of 4.2 ± 0.1, 5.2 ± 0.2 and 8.1 ± 0.4 at 1450, 3000 and 5100Å, respectively (red square in Figure 1). These results generally agree with bolometric correction from SSRQ200.

2.3 Eddington Ratio

For SS200, the accretion rate relative to the Eddington rate (the Eddington ratio, λ_E) can be calculated given the bolometric luminosities derived in § 2.1, i.e.

$$\lambda_E = \frac{L_{bol}}{L_{Edd}} = \frac{L_{bol}}{\frac{4\pi G c m_p}{\sigma_e} M_{BH}} = \frac{L_{bol}}{1.26 \times 10^{38} (M_{BH}/M_\odot)}$$

The black hole mass (M_{BH}) and the corresponding Eddington ratio (λ_E) of the XC413 are listed in Table 1 (Full table available on-line). The median and ranges of these parameters are reported in Table 2.

2.4 Parameter Space Classification

The XCRQ407 sample spans a wide range of z, L_{bol}, M_{BH} and λ_E (Table 2, Figure 2). The redshift range is comparable to that of Spitzer-SDSS sample (R06), and the luminosity, black hole mass and Eddington ratio ranges are comparable to that of PG quasars (Sikora et al. 2007). The size of the XCRQ407 sample is more than double that of previous samples, and is an order of magnitude larger than the E94 sample. This large sample size spanning a wide range of the parameter spaces is useful to understand whether and how the properties of the SMBH affect the SED shape.

XCRQ407 is an X-ray-selected sample and so includes sources with large host galaxy contribution (Paper I). For this reason, we focus on the host-corrected SEDs of the SSRQ200. For comparison we also study the SEDs of the XCRQ407 before the host correction. The median values and ranges in z, L_{bol}, M_{BH} and λ_E are similar for the two sub-samples (Table 2).

We can now check the SED shape dependence on each physical parameter by dividing the samples into quartiles of quasar z, L_{bol}, M_{BH} and λ_E, as shown by the dashed red lines in Figure 2. The bin boundaries and number of sources in different bins are given in Table 4. With these divisions, different bins have a similar number of quasars to calculate the mean SED, and therefore the possible statistical differences between different bins are minimized.

3 MEAN QUASAR SED DEPENDENCY ON PHYSICAL PARAMETERS

We can look for trends in the SEDs by checking the mean SED shape diversity in different bins. For each of the z, L_{bol}, M_{BH} and λ_E bins the mean SED are calculated as in Paper I. Briefly we: (1) converted the flux densities at each frequency for each object to luminosity, using a ΛCDM Concordance Cosmology (Komatsu et al. 2009); (2) shifted them to the rest frame for each source; (3) corrected for the small Galactic extinction (E(B-V)≃0.017); (4) limited the variability by restricting the photometry data in use to 2004 - 2007; (5) corrected for broad emission line contributions, which can be significant in the intermediate width Subaru bands; (6) linearly interpolated the SED to a uniform frequency grid ($\Delta \log \nu = 0.02$); (7) calculated the mean SED at each $\log \nu$ grid point. To avoid the SED shape being dominated by the few luminous quasars in each bin, we also calculated the mean of the SED after normalizing the SED at $1\mu m$.

As the COSMOS optical and infrared data used here were taken over a 4 year interval, from 2004 to 2007, and the SDSS data for the field were taken as early as 2001, variability is common in the XC413 sample (Paper I). Salvato et al. (2009) defined a convenient variability parameter Υ (the rms of the magnitude offsets at the sampled epochs) to quantify the variability of the sources. Salvato et al. (2009) found that $\Upsilon > 0.25$ efficiently separates out variable XMM-COSMOS sources (including both point-like and extended sources). We plot the Υ histogram in the left panel of Figure 3 for both the XC413 (blue dashed line) and SSRQ200 (black solid line) sample. Half of the XC413 AGN (199/413) and SSRQ200 AGN (94/200) have $\Upsilon > 0.25$. As in Paper I,

Table 3. Bolometric Corrections for the SSRQ200 sample [1]

λ (μm)	logν (Hz)	All z BC	σ	$0.1<z<1.2$ BC	σ	$1.2<z<1.5$ BC	σ	$1.5<z<1.8$ BC	σ	$1.8<z<4.3$ BC	σ
9.48	13.5	6.69	4.80	6.60	4.11	6.84	4.95	5.76	3.45	7.59	6.23
7.53	13.6	6.25	4.02	6.74	3.97	6.71	4.18	5.45	2.99	6.13	4.76
5.98	13.7	6.26	3.73	6.98	3.96	6.67	3.81	5.57	2.83	5.82	4.11
4.75	13.8	6.33	3.60	7.01	3.80	6.72	3.64	5.74	2.82	5.85	3.98
3.77	13.9	6.41	3.50	6.73	3.34	6.89	3.69	6.00	3.03	6.04	3.90
3.00	14.0	6.25	3.38	6.12	3.20	6.41	3.20	6.19	3.29	6.27	3.88
2.38	14.1	5.80	3.04	5.82	3.21	5.86	2.86	5.32	2.19	6.22	3.74
1.89	14.2	6.02	3.62	6.34	5.05	6.35	3.25	5.37	2.23	6.03	3.41
1.50	14.3	6.80	4.61	7.13	7.16	7.27	3.84	5.98	2.57	6.83	3.55
1.19	14.4	7.49	4.73	7.97	7.16	8.43	4.55	6.60	2.75	6.98	3.01
0.95	14.5	8.62	8.80	9.81	14.01	10.48	9.58	7.25	2.94	6.92	2.89
0.75	14.6	8.32	14.40	11.30	28.08	8.25	4.90	6.83	2.44	6.90	3.30
0.60	14.7	7.54	12.40	10.96	24.12	7.29	3.54	5.70	2.10	6.23	2.86
0.48	14.8	6.40	4.29	7.77	7.07	6.93	3.12	5.41	1.96	5.49	2.71
0.38	14.9	5.43	2.11	5.98	1.89	6.26	2.63	4.90	1.60	4.58	1.73
0.30	15.0	5.02	2.43	5.71	1.89	5.87	3.56	4.54	1.76	3.93	1.38
0.24	15.1	5.31	3.41	6.14	3.24	6.44	5.08	4.55	1.89	4.10	1.79
0.19	15.2	5.58	5.19	6.87	4.79	6.90	8.47	4.64	2.12	3.91	1.74
0.15	15.3	5.33	6.22	7.01	6.54	6.58	9.69	4.03	2.63	3.71	2.13
0.12	15.4	5.72	6.36	7.20	7.75	6.81	9.18	4.74	2.62	4.14	2.49
0.09	15.5	7.28	6.97	8.00	7.57	7.35	8.77	5.83	3.00	7.99	7.20

[1] After host galaxy subtraction.

Table 4. Parameter Space Bins

bin	redshift	N XCRQ407	N SSRQ200	L_{bol}	N XCRQ407	N SSRQ200	M_{BH}	N SSRQ200	logλ_E	N SSRQ200
1	0.103–1.166	107	50	44.00–45.23	126	50	7.18–8.10	50	0.008– 0.057	50
2	1.166–1.483	72	50	45.23–45.56	99	50	8.10–8.39	50	0.057– 0.114	50
3	1.483–1.848	84	51	45.56–45.87	93	50	8.39–8.66	50	0.114– 0.252	50
4	1.848–4.256	144	49	45.87–46.91	89	50	8.66–9.34	50	0.252– 2.506	50

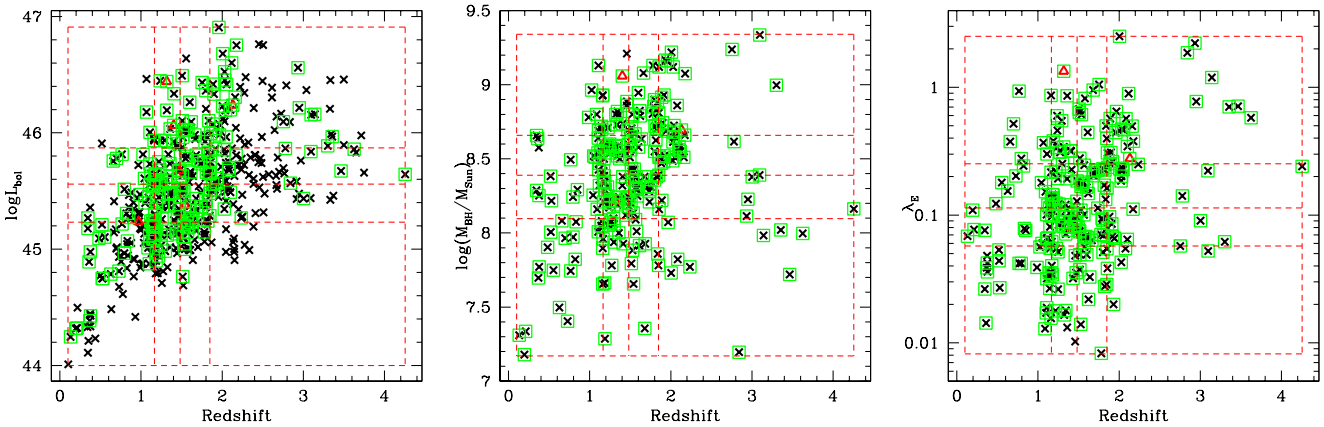

Figure 2. The classification of z, L_{bol}, M_{BH} and logλ_E bins of the XMM-COSMOS type 1 AGN sample. The dashed lines show the borders of quartile bins: the z bins ($0.1 \sim 1.2 \sim 1.5 \sim 1.8 \sim 4.3$), L_{bol} bins ($44.0 \sim 45.2 \sim 45.6 \sim 45.9 \sim 46.9$), M_{BH} bins ($7.2 \sim 8.1 \sim 8.4 \sim 8.7 \sim 9.4$) and λ_E bins ($0.008 \sim 0.057 \sim 0.114 \sim 0.252 \sim 2.506$). The black crosses show all the radio-quiet XMM-COSMOS type 1 AGN. The red triangles show the 6 radio-loud quasars. The green squares show the sub-sample SS203.

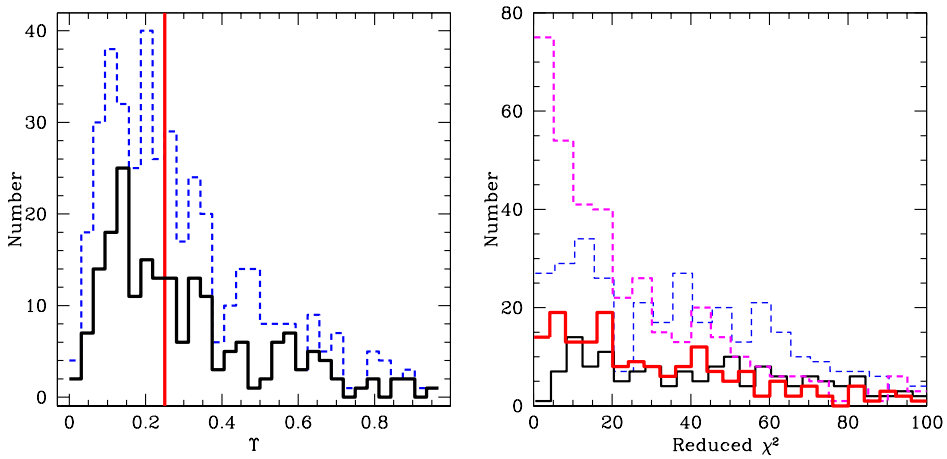

Figure 3. *Left:* Distribution of the variability parameter Υ (Salvato et al. 2009) of the SSRQ200 AGN (black solid line) and XC413 AGN (blue dashed line). The vertical red line divides the sources into variable (>0.25) and not-variable (<0.25). *Right:* The reduced χ^2 of the SED-fitting (see § 3 for details) both before (black solid line for SSRQ200 and blue dashed line for XC413) and after (red solid line for SSRQ200 and magenta dashed line for XC413) the restriction of the data to the 2004-2007 interval.

Table 5. Number of SSRQ200 quasars in Sub-bins for Partial Evolution

bin	sub-bin	z	L_{bol}	M_{BH}	λ_E
			N in sub-bin		
$z(2)$	1		9	11	11
	2		19	15	17
	3		14	13	14
	4		8	11	8
$z(3)$	1		10	11	11
	2		16	15	15
	3		10	15	11
	4		15	10	14
$\log L_{bol}(2)$	1	9		6	9
	2	19		17	19
	3	16		17	13
	4	6		10	9
$\log L_{bol}(3)$	1	10		15	10
	2	14		14	14
	3	10		10	12
	4	16		11	14
$\log M_{BH}(2)$	1	11	9		12
	2	15	17		23
	3	15	14		11
	4	9	10		4
$\log M_{BH}(3)$	1	11	15		10
	2	13	17		10
	3	15	10		19
	4	11	8		11
$\log \lambda_E(2)$	1	11	9	13	
	2	17	19	23	
	3	15	14	10	
	4	7	8	4	
$\log \lambda_E(3)$	1	8	11	8	
	2	14	13	11	
	3	11	12	19	
	4	17	14	12	

we do not use the Salvato et al. (2009) method to correct the SED, to avoid the modification to the SED shape. Alternatively, we restrict the data set to a shorter time period. Using χ^2 fits to the continuum (using quadratic functions to fit the observed data from rest frame 9000 Å to 912Å), we find that using only the data in the interval from 2004 to 2007 reduces the variability issue (right panel of Figure 3). The right panel of Figure 3 shows how the reduced time span improves χ^2 after applying these restrictions.

The resulting mean SEDs in different z and L_{bol} bins for XCRQ407 are shown in Figure 4. For ease of comparison, we also plot the E94 mean SED and a galaxy template from SWIRE (Polletta et al. 2007) normalized to the value of L_* from the UKIDSS Ultra Deep Survey (Cirasuolo et al. 2007, $M_K^* = -23$). The galaxy SED shown is an Elliptical galaxy with an age of 5 Gyr (hereafter E5). Different galaxy templates have similar shapes at around $1\mu m$, so here we just choose E5 as a representative case.

The SEDs in our sample have much less pronounced $1\mu m$ inflection point than in E94. In Paper I we concluded that this shape is probably due to the host galaxy contribution. It is clear from Figure 4 that for low z and low L_{bol} sources the galaxy component around $1\mu m$ strongly affects the shape of the SEDs. Indeed, at higher z and L_{bol}, the $1\mu m$ inflection becomes more obvious, as the quasar component becomes relatively stronger. However, even for high z and L_{bol} sources, the optical big blue bump is not as strong as in E94. This is probably because E94 considered a UV selected sample which picks out the bluest quasars (Schmidt & Green 1983). The mean SED shapes in the central z and L_{bol} bins are quite similar to the mean SEDs of all the quasars in XCRQ407.

For the SSRQ200 sample, we calculate the mean host-corrected SED for each bin, as shown in Figure 5 & 6. Even with the host-correction, the mean SEDs for the low z and L_{bol} sources are still relatively flat and different from E94. This may be due to insufficient host galaxy correction in some cases because of the scatter in the scaling relationship. The mean SEDs show that the top three bins of z and L_{bol}

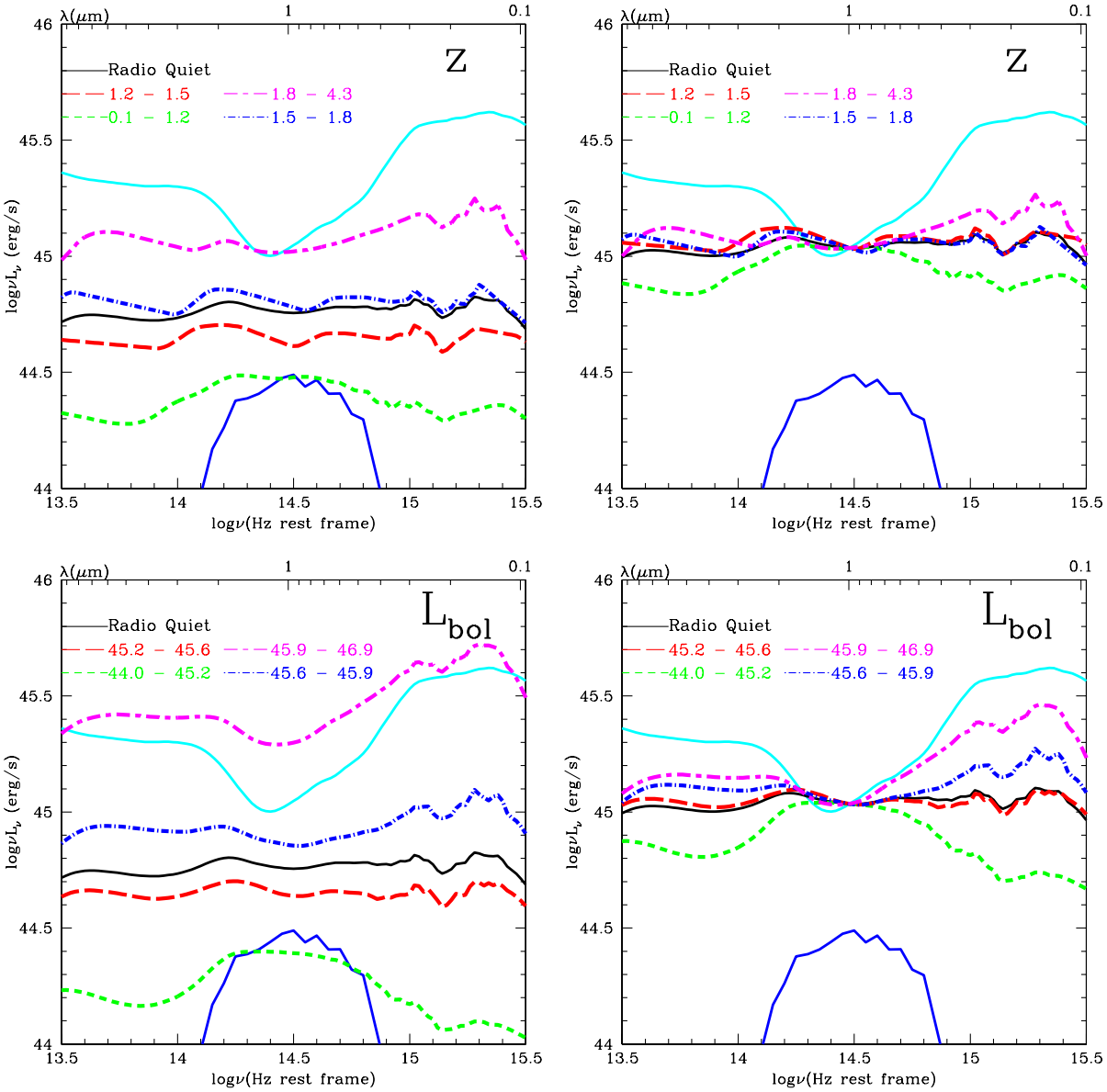

Figure 4. The mean SED for XCRQ407 in bins of z, L_{bol} before (left) and after (right) normalization at $1\mu m$ compared to E94 mean radio-quiet SED (cyan solid line). The black lines show the mean SED for all the radio-quiet type 1 AGN in the XMM-COSMOS sample (XCRQ407). A host galaxy template (an Elliptical (5 Gyr), E5, blue solid line) is normalized to L_* from UKIDSS Ultra Deep Survey (Cirasuolo et al. 2007).

have similar shapes, showing no sign of dependency on any of these parameters.

The 1 μm-normalized mean SED shapes of three M_{BH} bins are also similar to each other except for the second bin ($8.1 < \log(M_{BH}/M_{\odot}) < 8.4$). The optical slopes of the mean SEDs of different λ_E bins increase as λ_E increases, that is the mean SED is redder when the Eddington ratio is smaller. This trend is in agreement with the difference seen in typical quasar with $\lambda_E > 0.01$ and extremely low Eddington ratio AGN with $\lambda_E < 10^{-4}$ (Ho et al. 2008, Trump et al. 2011).

The z bins have the tightest distribution compared to other parameters (e.g., at $3\mu m$ and 3000Å the difference of the mean SEDs in different bins is 0.1 dex and 0.15 dex respectively, smaller than corresponding values of the other parameters). The difference of the mean SEDs in all the bins (except for the lowest bin) of each parameter are less than a factor of 2 even at the infared/UV end.

To check for partial dependencies of the SED shape on the physical parameters, we checked the SED shape difference with one parameter when fixing another. In order to have a large enough number of quasars in the mean SED calculation in each sub-bin, we consider the central two bins (Figure 7 & 8). The number of quasars in each sub-bin is listed in Table 5. As the number of quasars in each sub-bin is relatively small, these mean SEDs are more affected by particular SED shapes. In all these plots, the bottom / first bins are sometimes still affected by the host contribution,

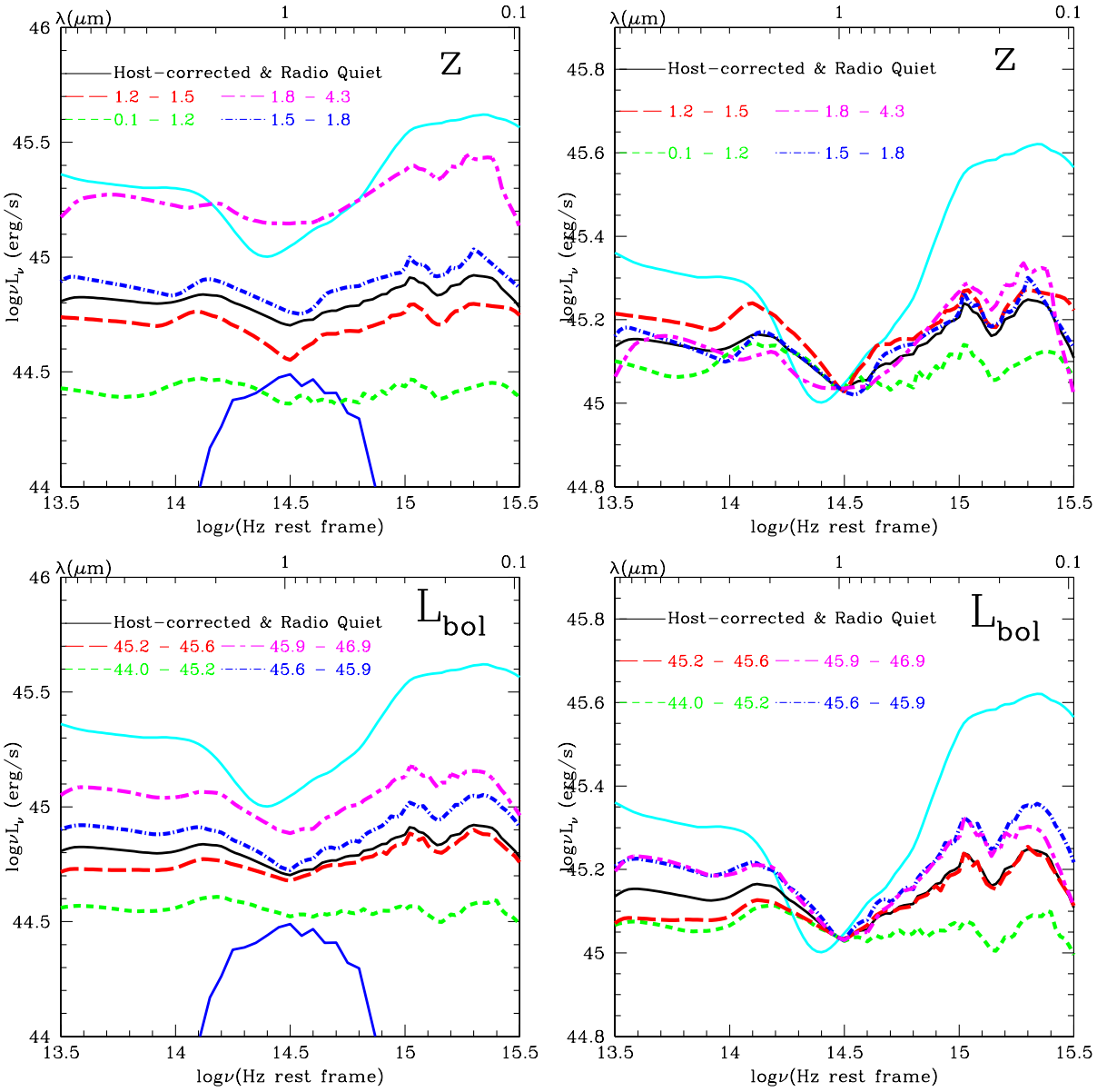

Figure 5. The host-corrected mean SED for SSRQ200 in bins of z and L_{bol} compared to E94 mean radio-quiet SED (cyan solid line):*left:* before normalization; *right:* normalized at $1\mu m$. The black solid lines show the host-corrected mean SED of all quasars in SSRQ200. A host galaxy template (an Elliptical (5 Gyr), blue solid line) is normalized to L_* from UKIDSS Ultra Deep Survey (Cirasuolo et al. 2007). Note that, to show the difference of the mean SEDs in different bins clearly, we expanded the y axis in all the plots of the right panel.

and the top / last bins are sometimes affected strongly by several specific SEDs (e.g. hot-dust-poor quasars, Hao et al. 2010, 2011). However, in general, the mean SEDs shapes in different sub-bins are very similar to each other and to the mean SED in that bin. For instance, when fixing z, the top / last two L_{bol}, M_{BH} or $\log \lambda_E$ sub-bins have a similar mean SED shape respectively.

As shown in the following section (§ 4), the dispersion of the SED in different bins ranges from 0.3 to 0.6, larger than the difference between the mean SED of adjacent bins; and the normalized SED dispersion can be as high as ~ 0.5 much larger than the difference between the mean normalized SED of adjacent bins (for details see § 4). The lack of SED shape dependency on z, L_{bol}, M_{BH} and λ_E we observed in the XCRQ407 and SSRQ200 suggests that neither the emission mechanism nor the accretion disk and torus structure alters systematically or dramatically with these parameters. In other words, a single intrinsic quasar SED in the optical/UV to near-infrared range is a meaningful concept. There is clearly still difference between individual SEDs, for example in the normalization due to L_{bol}. However, most of the differences in shapes are caused by different host contributions or reddening in quasars. The SED shape does not show a statistically significant dependence on the parameters we investigated.

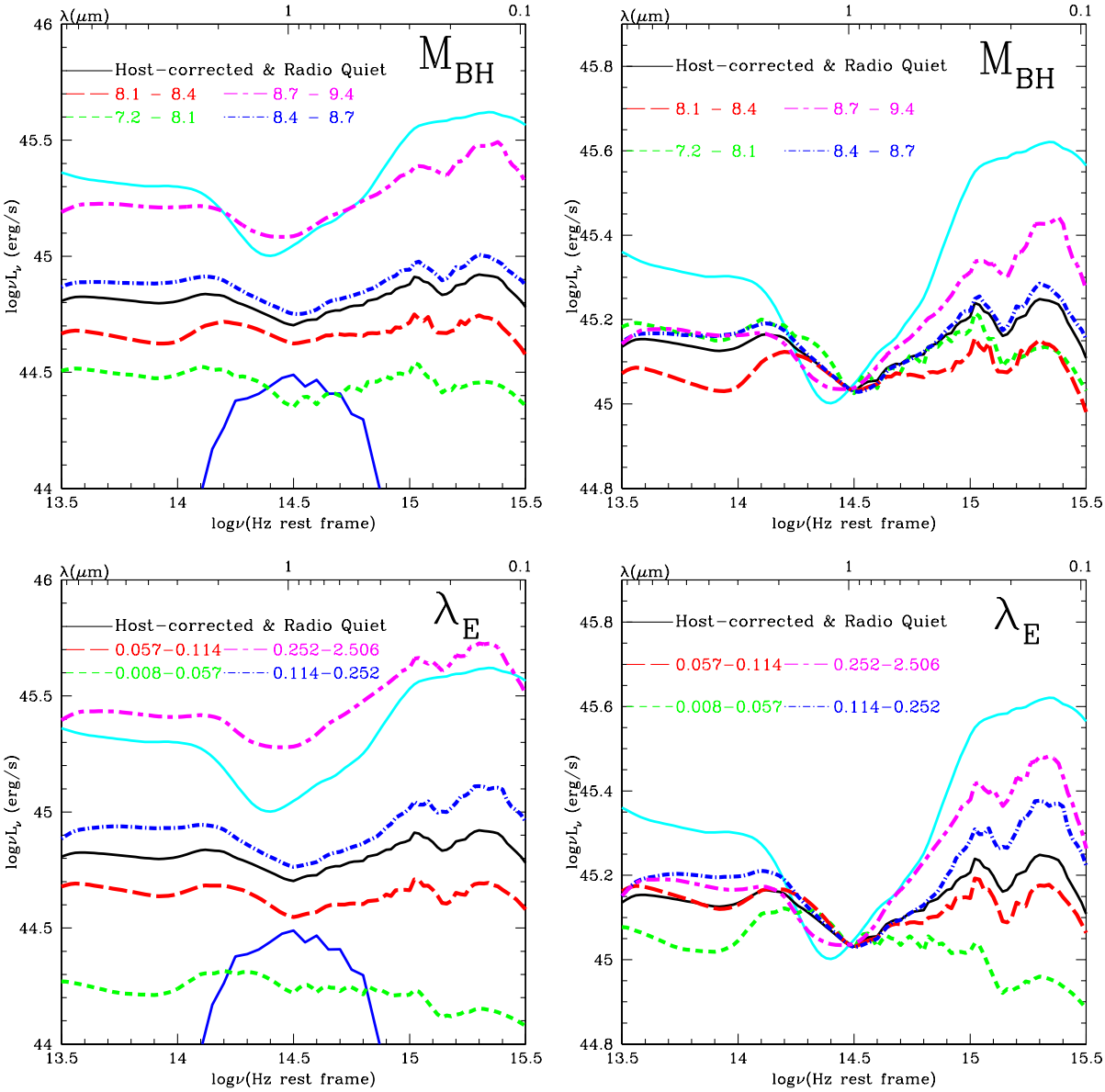

Figure 6. The host-corrected mean SED for SSRQ200 in bins of M_{BH} and λ_E compared to E94 mean radio-quiet SED (cyan solid line):*left:* before normalization; *right:* normalized at $1\mu m$. The black solid lines show the host-corrected mean SED of all quasars in SSRQ200. A host galaxy template (an Elliptical (5 Gyr), blue solid line) is normalized to L_* from UKIDSS Ultra Deep Survey (Cirasuolo et al. 2007). Note that, to show the difference of the mean SEDs in different bins clearly, we expanded the y axis in all the plots of the right panel.

Table 6. Bolometric Luminosity Dispersion in Each bin

sample bin	XCRQ407 z	XCRQ407 L_{bol}	SSRQ200 z	SSRQ200 L_{bol}	SSRQ200 M_{BH}	SSRQ200 λ_E
	$\sigma_{L_{bol}}$	$\sigma_{L_{bol}}$	$\sigma_{L_{bol}}$	$\sigma_{L_{bol}}$	$\sigma_{L_{bol}}$	$\sigma_{L_{bol}}$
1	0.46	0.50	0.45	0.50	0.36	0.26
2	0.38	0.38	0.35	0.38	0.38	0.10
3	0.42	0.43	0.41	0.43	0.43	0.09
4	0.42	0.49	0.39	0.48	0.39	0.25

4 SED DISPERSION DEPENDENCY ON PHYSICAL PARAMETERS

Even if the mean SEDs show little or no dependency on physical parameters, the SED dispersion may change with them. We checked the SED dispersion in different bins for both the XCRQ407 and SSRQ200 by calculating the dispersion of νL_ν at each frequency in each bin. The dispersion of the SEDs could purely / mostly caused by the luminosity difference among quasars in each bin. In order to distinguish the dispersion caused by different brightness of quasars and the SED shape dispersion, we consider the dispersion of the SEDs before and after normalizing all the SEDs at $1\mu m$ (Figure 9-11). The bolometric luminosity dispersion in each

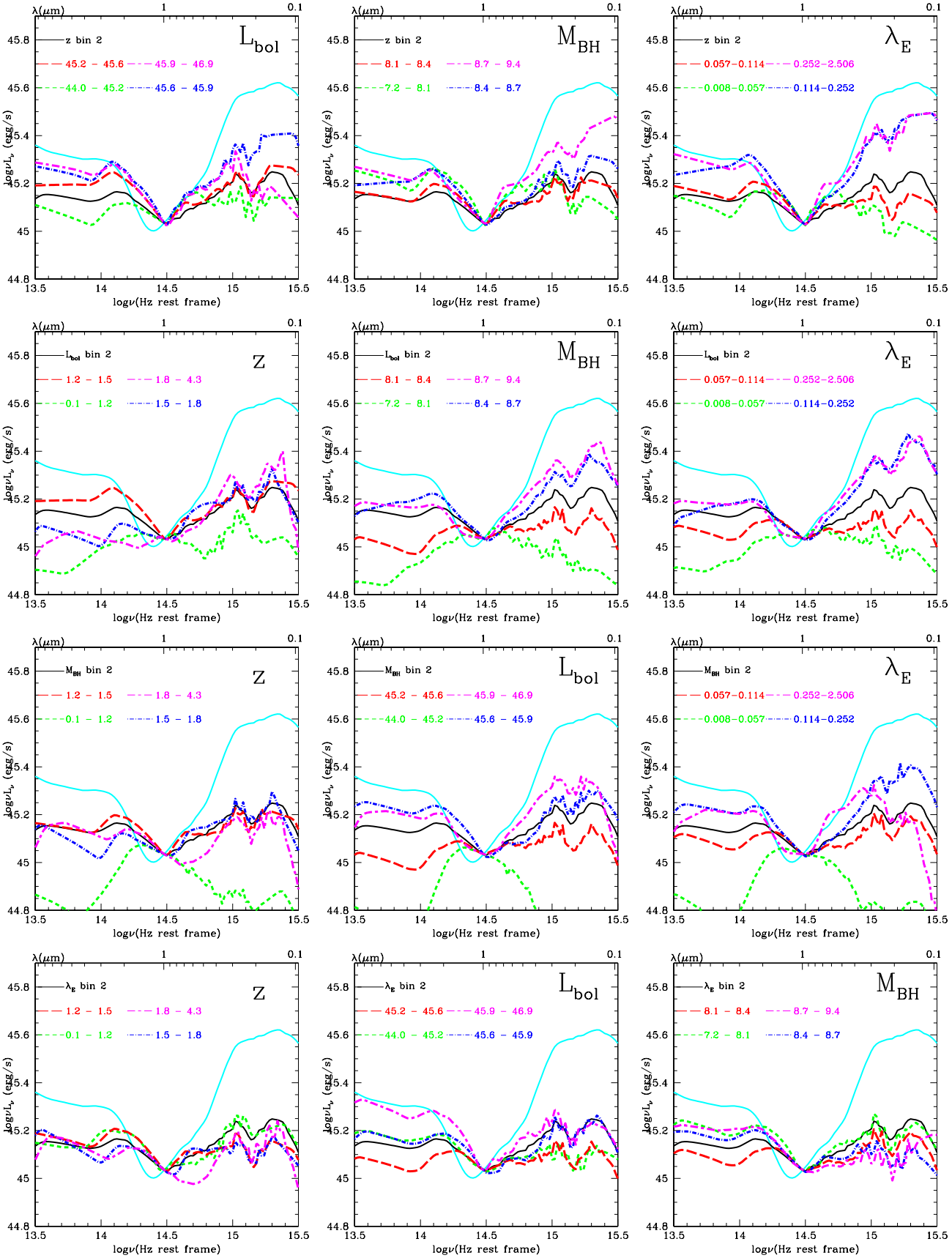

Figure 7. The mean host-subtracted SED normalized at $1\mu m$ compared to E94 mean radio-quiet SED (cyan solid line). Different rows are for quasars in specific bins: (1) z bin 2 ($1.2 < z < 1.5$); (2) $\log L_{bol}$ bin 2 ($45.2 < \log L_{bol} < 45.6$); (3) $\log(M_{BH}/M_{\odot})$ bin 2 ($8.1 < \log(M_{BH}/M_{\odot}) < 8.4$); (4) $\log \lambda_E$ bin 2 ($0.057 < \lambda_E < 0.114$). The symbol on the upper right corner of the each plot shows which sub-bin is considered. The lines are color coded as in Figure 5 & 6.

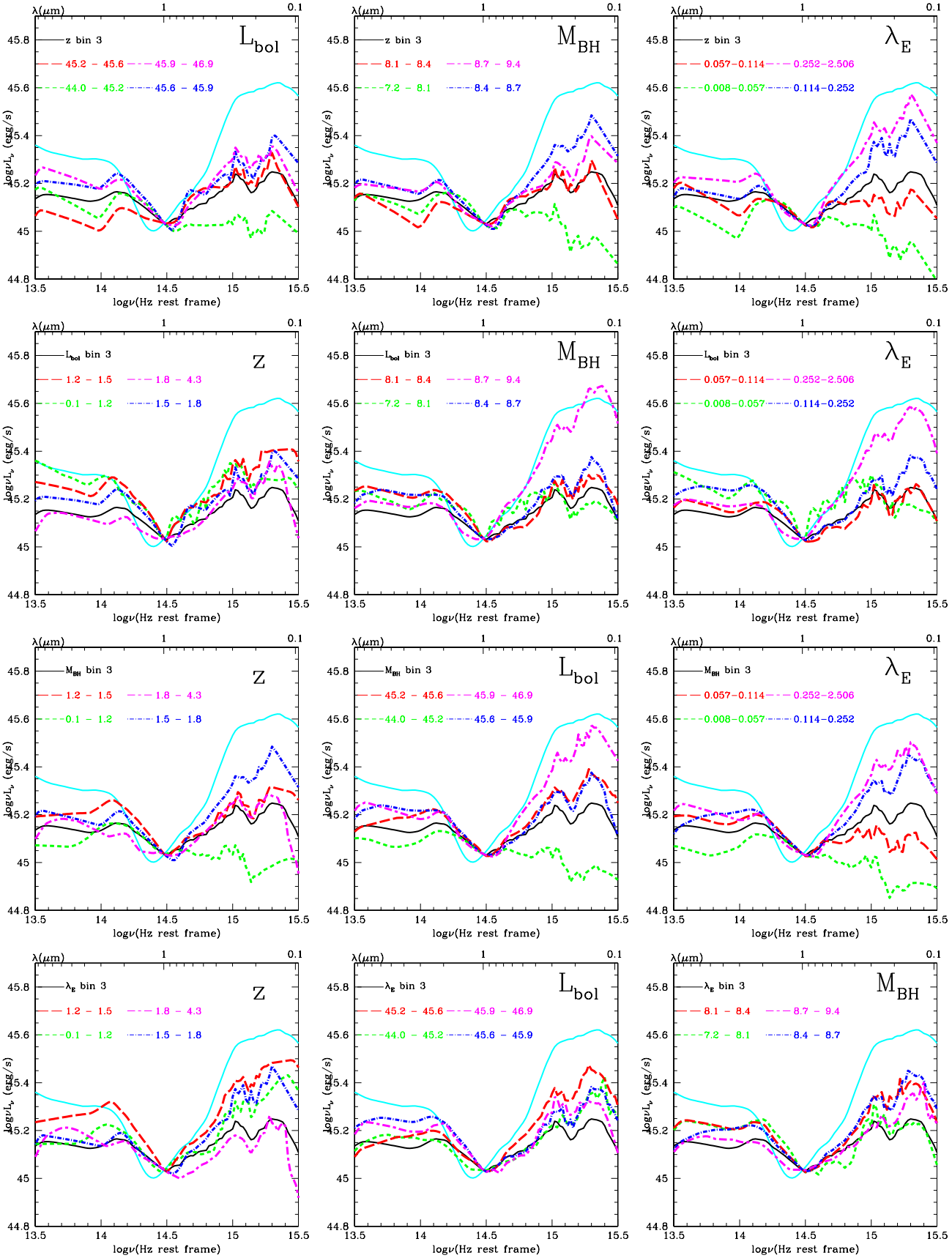

Figure 8. The mean host-subtracted SED normalized at $1\mu m$ compared to E94 mean radio-quiet SED (red solid line). Different rows are for quasars in specific bins: (1) z bin 3 ($1.5 < z < 1.8$); (2) $\log L_{bol}$ bin 3 ($45.6 < \log L_{bol} < 45.9$); (3) $\log(M_{BH}/M_{\odot})$ bin 3 ($8.4 < \log(M_{BH}/M_{\odot}) < 8.7$); (4) $\log \lambda_E$ bin 3 (right half, $0.114 < \lambda_E < 0.252$). The symbol on the upper right corner of the each plot shows which sub-bin is considered. The lines are color coded as in Figure 5 & 6.

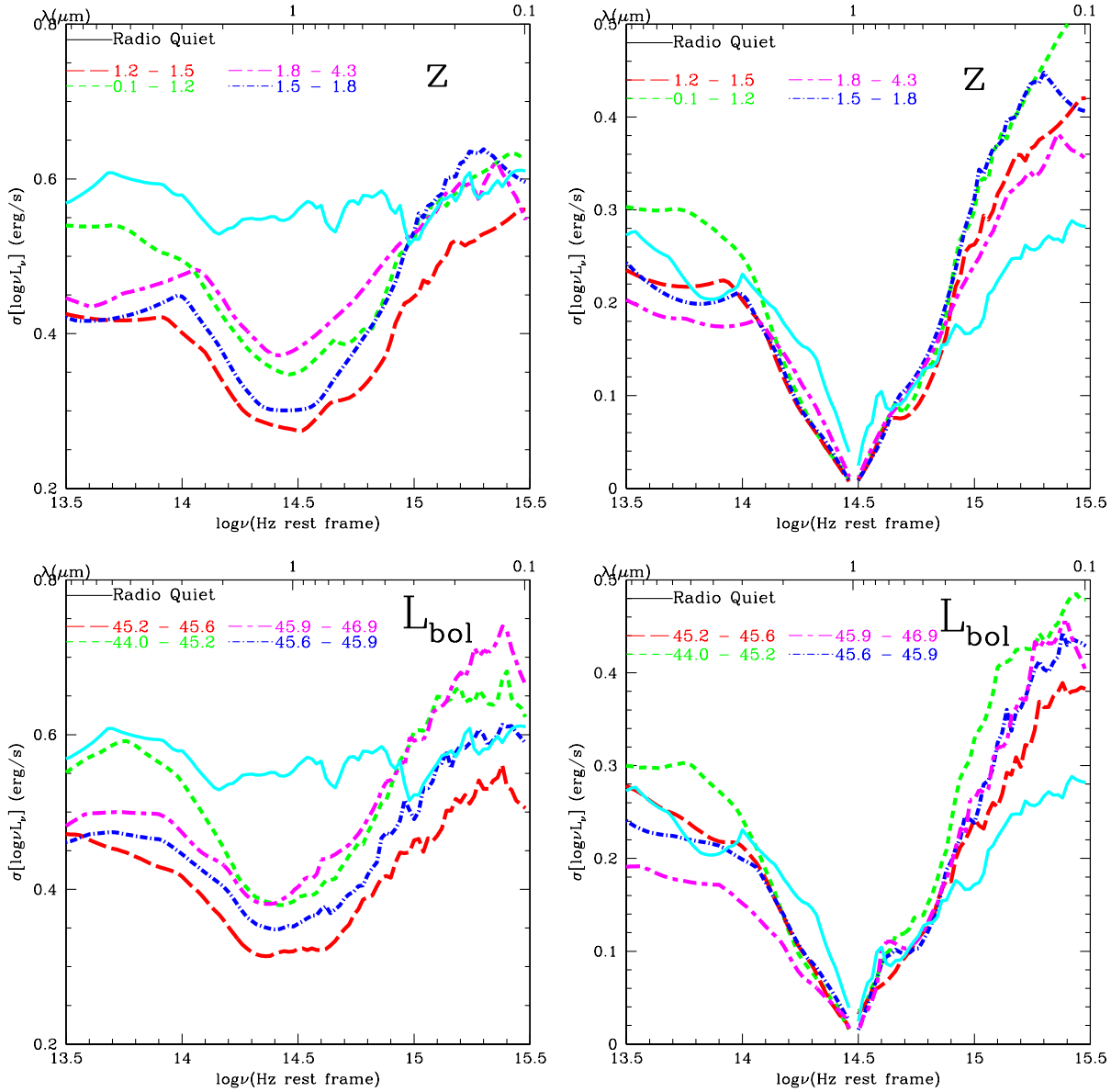

Figure 9. The dispersion of the SEDs for XCRQ407 in bins of z and L_{bol} before (left) and after (right) normalization at $1\mu m$ compared to corresponding E94 radio-quiet SED dispersion (cyan solid curve).

bin is listed in Table 6. From the left panels of Figure 9-11 and Table 6, we can see majority of the SED dispersion is caused by the luminosity dispersion within bins. For the λ_E bins, the quasar brightness effect is the least. So we will concentrate on the dispersion of the normalized SEDs (right panel of Figure 9-11) to see if there is any SED dispersion dependency on physical parameters. The normalized SED dispersion in different bins at certain specific wavelengths are listed as examples in Table 7.

The resulting dispersion of normalized SEDs in z and L_{bol} bins for XCRQ407 compared to E94 radio-quiet SED dispersion are shown in right panel Figure 9. The XMM-COSMOS SEDs generally have a larger dispersion in the optical to UV range compared to E94 radio-quiet sample. This is probably because E94 is biased toward blue quasars, unlike the XMM selected XCRQ407, thus it does not include quasars with various optical shapes/colors. The 1–10 μm dispersion of XCRQ407 is closely similar to E94, except at $\sim 2\mu m$, where it is somewhat lower. The XMM-COSMOS SED dispersion is quite similar in the 3 μm to 3000 Å range for different z or L_{bol} bins. The SED dispersions in this range are all below a factor of 2.

For the host-corrected SSRQ200 sample, the dispersion of the SED for each bin is shown in Figure 10 & 11. The SED dispersion in the 3 μm to 3000 Å range is not as tight as the un-corrected sample, implying extra dispersion induced by the host-correction process depends on z, L_{bol}, M_{BH} or λ_E. The lowest bin for each parameter always has the largest dispersion in most frequency range in all the dispersion plots.

In all these SED dispersion plots, the UV (at $\sim 0.1\mu m$) dispersion is generally larger than the near-IR (at $\sim 10\mu m$) dispersion. This could mean that the reprocessing of the

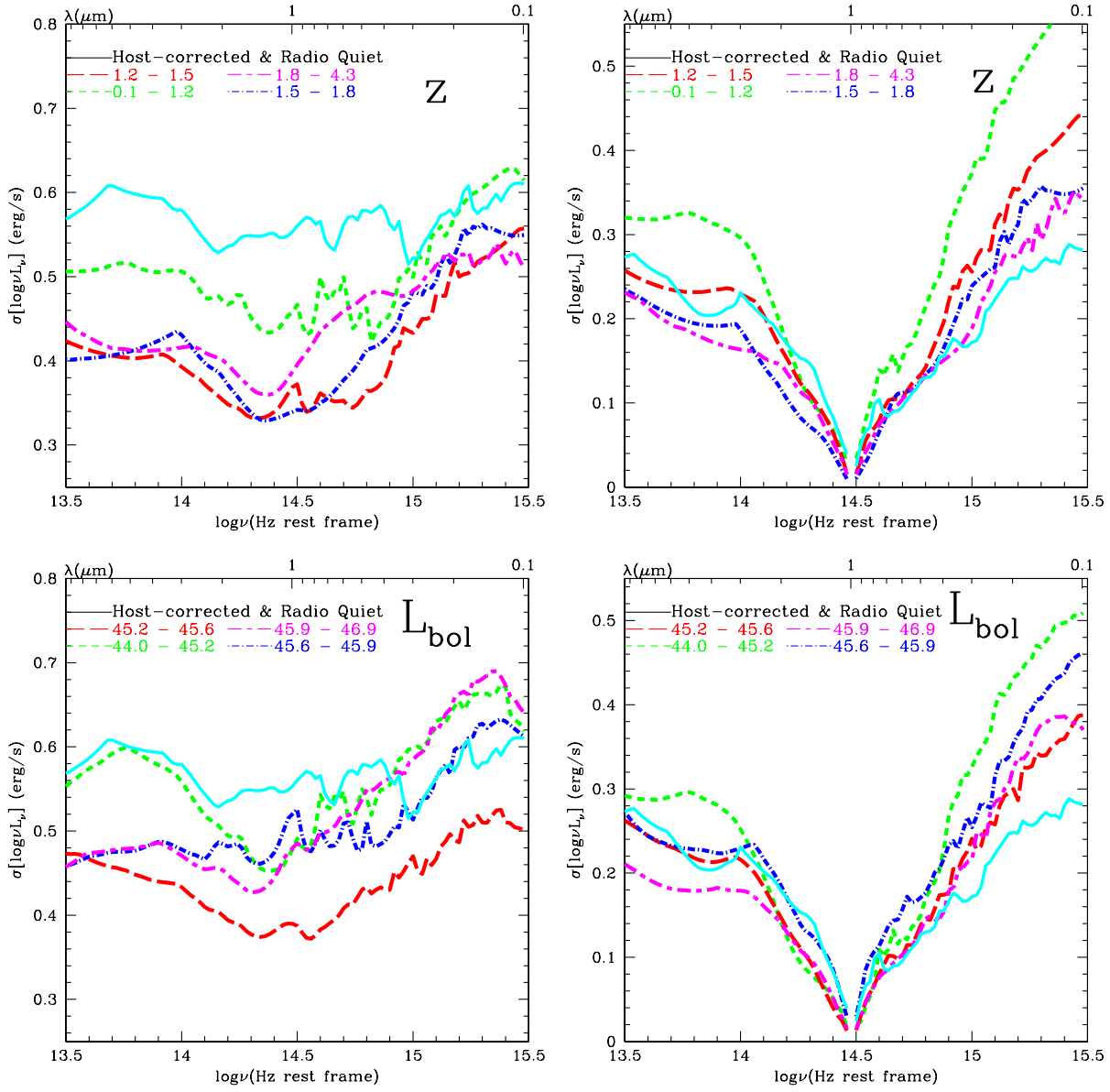

Figure 10. The dispersion of host-subtracted SEDs for SSRQ200 in bins of z and L_{bol} before (left) and after (right) normalized at $1\mu m$ compared to corresponding E94 radio-quiet SED dispersion (cyan solid curve).

hot dust component has slightly smoothed the discrepancy of the accretion disk emission. Alternatively, this could be completely caused by the variability of the quasar which affects the UV SED most, or by reddening.

We can compare the difference between mean SEDs in § 3 and the SED dispersion discussed above. Before normalization, the SED dispersion is comparable and slightly larger than the mean SED difference between adjacent bins. As majority of the difference and dispersion is caused by the bolometric luminosity distribution, we will focus our comparison for the normalized SEDs. The normalized SED dispersion can reach up to ~ 0.5. At each frequency, the dispersion is much larger than the normalized mean SED difference. We could thus state that the mean SEDs are invariant within 1σ (at most frequencies $> 2\sigma$).

5 DISCUSSION AND CONCLUSION

We analyzed the dependence of both the mean and dispersion of the SED shapes in the optical-UV to IR range on the parameters z, L_{bol}, M_{BH} and λ_E for the 407 XMM-COSMOS radio-quiet type 1 AGN sample. We also calculated the bolometric correction at UV-optical to near-IR for the host-corrected SSRQ200, and in four different redshift bins. The bolometric correction for different redshift bins are quite similar to each other.

As the XMM-COSMOS quasar sample is an X-ray-selected sample, it includes also sources with low nucleus to host contrast. The mean SED of the whole sample is greatly affected by the host galaxy emission for low redshifts and luminosities. Therefore, we mainly studied the mean and dispersion SEDs of a host-corrected sub-sample

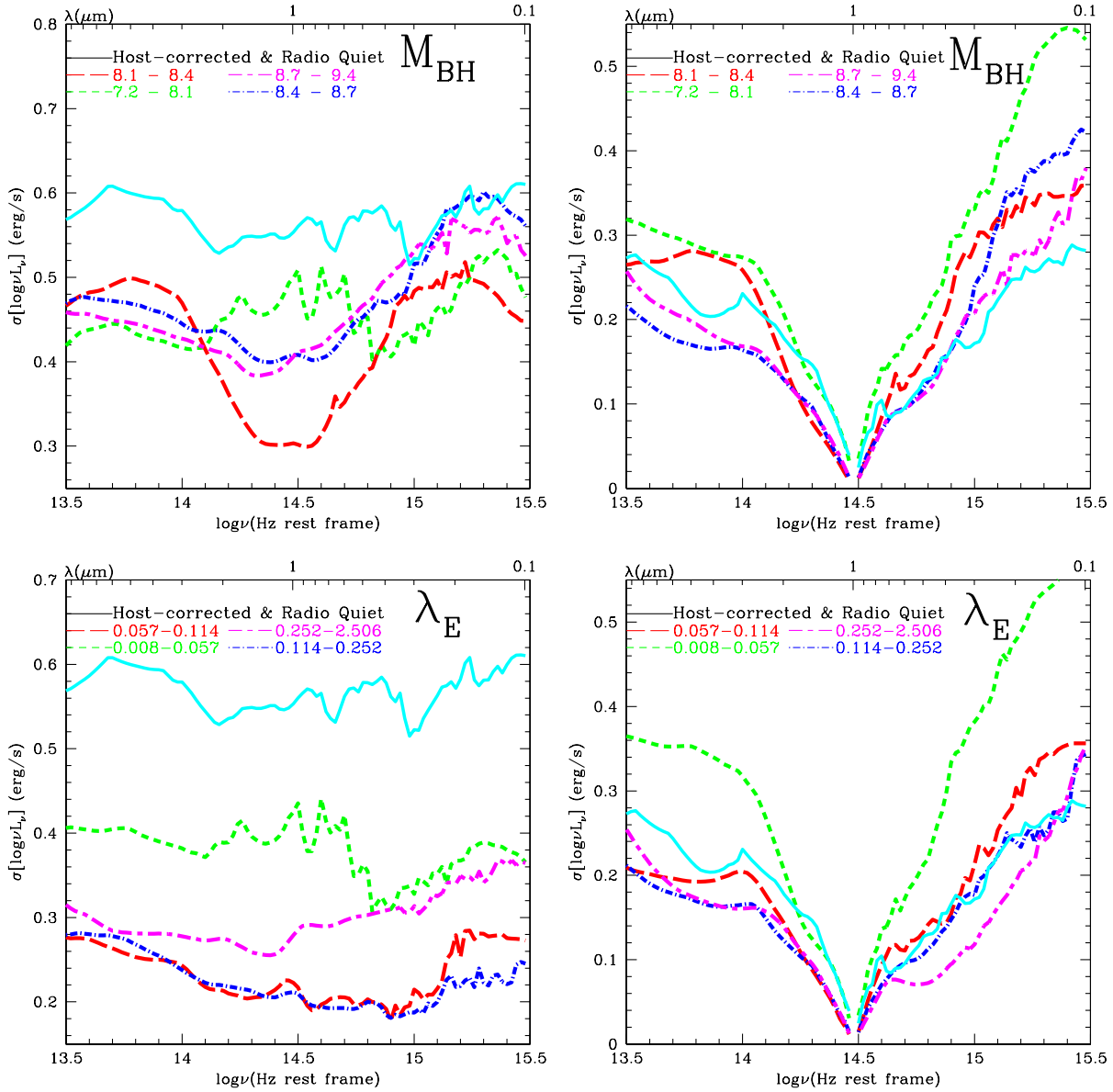

Figure 11. The dispersion of host-subtracted SEDs for SSRQ200 in bins of M_{BH} and λ_E before (left) and after (right) normalized at $1\mu m$ compared to corresponding E94 radio-quiet SED dispersion (cyan solid curve).

of 200 radio-quiet quasars, SSRQ200, in four quartile bins of z, L_{bol}, M_{BH} and λ_E. The mean SED shapes in the different bins are quite similar to each other. These SEDs are also generally similar to the E94-like mean SED shape, but they tend to have less pronounced optical to UV bump emission than in E94, as E94 is biased towards blue quasars. Even if we fix one parameter (e.g. redshift), the mean SEDs show no statistical significant evolution with the others.

We checked the dispersion of SEDs in different parameter bins. The near-IR SED dispersion is generally smaller compared to the UV SED dispersion, which might be due to the variability of the quasar that mainly affects UV SED. The SEDs before and after host correction have very similar dispersion in the 3 μm to 3000 Å range for different bins, which implies an invariant intrinsic dispersion of SED shapes in this wavelength range. However, in this wavelength range, the host-corrected SED dispersion is not as tight as the uncorrected sample, probably due to the extra dispersion induced by the scaling relationship depends on the physical parameters. When we compare the SED dispersion with the difference of the mean SEDs, we could conclude that the mean SED is invariant within 1σ (at most frequencies more than 2σ).

There is no statistical significant dependency of the mean SED with z, L_{bol}, M_{BH} or $\log \lambda_E$. This result implies that the global quasar structures (the accretion disk and the torus) are invariant with respect to these parameters. Despite the strong expectation that feeding of the AGN and host galaxy is likely to change (e.g. Merloni et al 2010), as well as the X-ray corona is likely to change (α_{OX} varies with λ_E, e.g. Lusso et al. 2010), the accretion disk and the torus

Table 7. Normalized SED Dispersions at Certain Wavelength

bin	sub-bin	Wavelength 10 μm	3 μm	3000Å	2500Å	1000Å
	1	0.30	0.25	0.30	0.36	0.50
XCRQ407	2	0.24	0.20	0.26	0.30	0.42
z	3	0.24	0.21	0.31	0.37	0.41
	4	0.20	0.18	0.24	0.28	0.35
	1	0.30	0.24	0.33	0.38	0.48
XCRQ407	2	0.28	0.21	0.24	0.26	0.38
$\log L_{bol}$	3	0.24	0.20	0.24	0.30	0.43
	4	0.19	0.15	0.26	0.31	0.40
	1	0.32	0.30	0.37	0.42	0.57
SSRQ200	2	0.26	0.23	0.26	0.28	0.44
z	3	0.24	0.19	0.24	0.26	0.36
	4	0.23	0.16	0.19	0.24	0.34
	1	0.29	0.25	0.33	0.37	0.51
SSRQ200	2	0.26	0.22	0.24	0.26	0.39
$\log L_{bol}$	3	0.27	0.23	0.25	0.28	0.46
	4	0.21	0.18	0.22	0.27	0.37
	1	0.32	0.27	0.33	0.37	0.53
SSRQ200	2	0.26	0.26	0.29	0.31	0.36
$\log M_{BH}$	3	0.22	0.16	0.24	0.30	0.42
	4	0.26	0.17	0.21	0.23	0.38
	1	0.36	0.32	0.38	0.42	0.56
SSRQ200	2	0.21	0.20	0.21	0.23	0.36
$\log \lambda_E$	3	0.21	0.17	0.18	0.21	0.34
	4	0.25	0.16	0.12	0.15	0.35

seem to not depend on this mechanism. Thus an intrinsic SED in UV-optical to near-IR exists.

The differences among the SEDs show there might be diversity only at the second order. Host contamination, reddening and quasar variability should lead to a dispersion in the UV and near-IR SEDs. The lack of SED dispersion evolution indicates that these effects themselves do not show much systematic dependence on physical parameters.

All the above conclusions depend on the reliability of the host correction process. This assumes the scaling relationship between black hole mass and bulge mass (e.g. Marconi & Hunt 2003) with an evolutionary term (Bennert et al. 2010, 2011). The black hole mass estimates can lead to a dispersion as large as 0.4 (e.g., Vestergaard & Peterson 2006) besides dispersion of the relationship itself. The evolution of this relationship is still under debate (see e.g., Schramm & Silverman 2013). Uncertainties in this correlation might limit our ability to detect SED shape dependency on physical parameters and it is hard to estimate the exact amount of dispersion associated with the host correction process.

A less model dependent analysis will be described in a following paper (Hao et al. 2013a), where we introduce a new mixing diagram to readily distinguish different SED shape, i.e. galaxy-dominated, quasar-dominated and reddening dominated SEDs.

So far, we have only studied the SED shape one decade on either side of $1\mu m$. To study the SED shape evolution in UV or FIR is less easy. The UV is greatly affected by both reddening and variability that is different for different sources. The FIR is greatly affected by host galaxy star formation, which also varies from case to case. We will discuss these two regions of the quasar SED in following papers.

ACKNOWLEDGMENTS

HH thanks Belinda Wilkes and Martin J. Ward for discussion. This work was supported in part by NASA *Chandra* grant number G07-8136A (HH, ME, FC) and the Smithsonian Scholarly Studies (FC). Support from the Italian Space Agency (ASI) under the contracts ASI-INAF I/088/06/0 and I/009/10/0 is acknowledged (AC and CV). MS acknowledges support by the German Deutsche Forschungsgemeinschaft, DFG Leibniz Prize (FKZ HA 1850/28-1). KS gratefully acknowledges support from Swiss National Science Foundation Grant PP00P2_138979/1.

REFERENCES

Appleton, P. N., et al., 2004, ApJS, 154, 147
Barth, A. J., Martini, P., Nelson, C. H., Ho, L. C. 2003, ApJL, 594, 95
Bennert, V. N., Treu, T., Woo, J.-H., Malkan, M. A., Le Bris, A., Auger, M. W., Gallagher, S., Blandford, R. D., 2010, ApJ, 708, 1507
Bennert, V. N., Auger, M. W., Treu, T., Woo, J.-H., Malkan, M. A., 2011, ApJ, 742, 107
Brandt, W. N., et al. 2002, ApJL, 569, 5
Brusa, M. et al. 2009, ApJ, 693, 8
Brusa, M., et al., 2010, ApJ, 716, 348
Cappelluti, N., et al., 2007, ApJS, 172, 341
Cappelluti, N., et al., 2009, A&A, 497, 635
Cirasuolo, M. et al. 2007, MNRAS, 380, 585
Civano, F., et al., 2011, ApJ, 741, 91
Cowie, L. L., et al. 2003, ApJ, 584, L57
Czerny, B., & Elvis, M., 1987, 321, 305
Dunne, L. & Eales, S. A. 2001, MNRAS, 327, 697
Elvis, M. et al., 1994, ApJS, 95, 1
Elvis, M. et al., 2012, ApJ, 759, 6
Ferrarese, L. & Merrit, D. 2000 ApJ, 539, L9
Fiore, F. et al. 2003, A&A, 409, 79
Gebhardt, K., et al., 2000, ApJ, 539, L13
Goldschmidt, P., Kukula, M. J., Miller, L., & Dunlop, J. S., 1999, ApJ, 511, 612
Haardt, F., & Maraschi, L. 1991, ApJ, 380, L51
Hao, H., et al., 2010, ApJ, 724, L59
Hao, H., et al., 2011, ApJ, 733, 108
Hao, H., et al., 2013, MNRAS, submitted, arXiv:1210.3044
Hao, H., et al., 2013, in preparation
Harris, D. E., & Krawczynski, Henric, 2006, ARA&A, 44, 463
Hasinger, G., et al., 2007, ApJS, 172, 29
Ho, L. C., 1999, ApJ, 516, 672
Ho, L. C., 2005, ApJ, 629, 680
Ho, L. C., 2007, ApJ, 669, 821
Ho, L. C., 2008, ARA&A, 46, 475
Hopkins, P., Richards, G. T., & Hernquist, L., 2007, ApJ, 654, 731
Ivezić, Ž., 2004, in Multiwavelength AGN Surveys, ed. R.Mújica & R. Maiolino (Singapore: World Scientific), 53
Jiang, L. et al., 2006, AJ, 132, 2127

Jiang, L., Fan, X., Vestergaard, M., Kurk, J. D., Walter, F., Kelly, B. C., & Strauss, M. A., 2007, AJ, 134, 1150
Just, D. W., Brandt, W. N. et al., 2007, ApJ, 665, 1004
Kawaguchi, T., Shimura, T., & Mineshige, S. 2001, ApJ, 546, 966
Komatsu, E., et al., 2009, ApJS, 180, 330
Kormendy, J. & Richstone, D. 1995, ARA&A, 33,581
Kurk, J. D. et al. 2007, ApJ, 669, 32
Laor, A., Netzer, H., & Piran, T. 1990, MNRAS, 242, 560
Laor, A., Fiore, F., Elvis, M., Wilkes, B. J., Mcdowell, J. C. 1997, ApJ, 477, 93
Lapi, A. et al. 2011, ApJ, 742, 24
Lilly, S. J., et al., 2007, ApJS 172, 70
Lilly, S. J., et al., 2009, ApJS 184, 218
Lusso, E., et al., 2010, A&A 512, 34
Magorrian, J., et al., 1998, AJ, 115, 2285
Mainieri, V., et al., 2007, ApJS, 172, 368
Marconi, A. & Hunt, L. K. 2003, ApJ 589, L21
Mateos, et al. 2005, A&A, 433, 855
Mathur,S., Wilkes, B. J. & Ghosh, H. 2002, ApJL, 570, 5
McAlary, C. W. & Rieke, G. H. 1988, ApJ, 333, 1
McLure, R. J. & Jarvis, M. J., 2002, MNRAS, 337, 109
Menci, N., et al. 2008, ApJ, 686, 219
Merloni, A., et al. 2010, ApJ 708, 137
Mortlock, D. J., et al., 2011, Nature, 474, 616
Mullaney, J. R., et al. 2012, MNRAS, 419, 95
Netzer, H. et al. 2007 ApJ, 666, 806
Peng, C. Y., Impey, C. D., Rix, H.-W., Kochanek, C. S., Keeton, C. R., Falco, E. E., Lehár, J., McLeod, B. A. 2006, ApJ, 649, 616
Polletta, M. et al. 2007, ApJ, 663, 81
Rees, M.J. 1984, ARA&A, 22, 471
Richards, G. T. et al. 2006, ApJS, 166, 470
Richstone, D., et al. 1998, Nature, 395, 14
Runnoe, J. C., Brotherton, M. S., Shang, Z., et al., 2012, MNRAS, 422, 478
Sanders, D. B., Phinney, E. S., Neugebauer, G., Soifer, B. T., & Matthews, K. 1989, ApJ, 347, 29
Schmidt, M. & Green, R. F., 1983, ApJ, 269, 352
Schneider, D. P. et al. 2007, AJ, 134, 102
Schramm, M. & Silverman, J. D., 2013, ApJ, 767, 13
Scoville, N. Z., et al., 2007, ApJS, 172, 1
Shakura, N. I., & Sunyaev, R. A., 1973, A&A, 24, 337
Shang, Z., et al., 2011, ApJS, 196, 2
Sikora, M., Stawarz, L. & Lasota, J. P., 2007, ApJ, 658, 815
Silverman, J. D. et al. 2002, ApJL, 569, 1
Silverman, J. D. et al. 2005, ApJ, 624, 630
Shields, G. A., Menezes, K. L., Massart, C. A., Vanden Bout, P. 2006, ApJ, 641, 683
Soltan, A. 1982, MNRAS, 200, 115
Steffen, A. T., Strateva, I., et al., 2006, AJ, 131, 2826
Steinhardt, C. L. & Elvis, M. 2010, MNRAS, 402, 2637
Stocke, J. T., Morris, S. L., Weymann, R. J. & Foltz, C. B., 1992, ApJ, 396, 487
Suganuma, M. et al. 2006, ApJ, 639, 46
Terashima, Y. & Wilson, A. S. 2003, ApJ, 583, 145
Tremaine, S., et al. 2002, ApJ, 574, 740
Trump, J.R. et al. 2009a ApJ, 696, 1195
Trump, J.R. et al. 2009b ApJ, 700, 49
Trump, J. R. et al. 2011 ApJ, 733, 60
Ueda, Y. et al. 2003 ApJ 598, 886
Vestergaard, M. 2004, ApJ, 601, 676
Vestergaard, M. & Peterson, B. M. 2006 ApJ 641, 689
Vignali, C., Brandt, W. N., Schneider, D. P. 2003a, AJ, 125, 433
Vignali, C. et al. 2003b, AJ, 125, 2876
Wilkes, B. J., 2003, ASPC, 311, 37
Wilkes, B. J. & Elvis, M., 1987, ApJ, 323, 243
Williams, O. R., et al., 1992, ApJ, 389, 157
Young, M., Elvis, M., Risaliti, G., 2010, AJ, 708, 1388
Zamorani, G., Henry, J.P., Maccacaro, T., et al. 1981, ApJ, 245, 357
Zdziarski, A. A., Poutanen, J., & Johnson, W. N. 2000, ApJ, 542, 703